

A Compact Supermassive Binary Black Hole System

C. Rodriguez^{1,2}, G. B. Taylor^{1,3}, R. T. Zavala⁴, A. B. Peck⁵, L. K. Pollack⁶ & R. W. Romani⁷

ABSTRACT

We report on the discovery of a supermassive binary black hole system in the radio galaxy 0402+379, with a projected separation between the two black holes of just 7.3 pc. This is the closest black hole pair yet found by more than two orders of magnitude. These results are based upon recent multi-frequency observations using the Very Long Baseline Array (VLBA) which reveal two compact, variable, flat-spectrum, active nuclei within the elliptical host galaxy of 0402+379. Multi-epoch observations from the VLBA also provide constraints on the total mass and dynamics of the system. Low spectral resolution spectroscopy using the Hobby-Eberly Telescope indicates two velocity systems with a combined mass of the two black holes of $\sim 1.5 \times 10^8 M_{\odot}$. The two nuclei appear stationary while the jets emanating from the weaker of the two nuclei appear to move out and terminate in bright hot spots. The discovery of this system has implications for the number of close binary black holes that might be sources of gravitational radiation. Green Bank Telescope observations at 22 GHz to search for water masers in this interesting system are also presented.

Subject headings: galaxies: active – galaxies: individual (0402+379) – radio continuum: galaxies – radio lines: galaxies

¹Department of Physics and Astronomy, University of New Mexico, Albuquerque, NM 87131

²Department of Physics, Universidad Simon Bolivar, Sartenejas, Venezuela

³National Radio Astronomy Observatory, Socorro NM 87801

⁴United States Naval Observatory, Flagstaff Station 10391 W. Naval Observatory Rd. Flagstaff, AZ 86001

⁵Harvard-Smithsonian CfA, SMA Project, 645 N. A'ohoku Pl, Hilo, HI 96721

⁶Department of Astronomy & Astrophysics, University of California at Santa Cruz, Santa Cruz, CA 95064

⁷Department of Physics, Stanford University, Stanford, CA 94305-4060

1. Introduction

Black holes are a direct consequence of the physics described in Einstein’s theory of gravity. There is a great deal of indirect astronomical observational evidence for these exotic objects in two mass ranges: stellar mass black holes, with masses of 4-15 times the mass of our Sun; and supermassive black holes, with masses ranging from 10^5 to 10^{10} solar masses. There is also some evidence for intermediate-mass black holes, those with masses of a few hundred to a few thousand solar masses (see Filippenko & Ho 2003 , Gebhardt et al. 2005).

Since most nearby galaxies harbor supermassive black holes at their centers (Richstone et al. 1998), the merging of galaxies, an essential part of the galaxy formation process, is thought to be the prevalent method in which supermassive black hole binaries are formed. Accordingly, such systems should be common in galaxies. An understanding of the evolution and formation of these systems is important for an understanding of the evolution and formation of galaxies in general.

The evolution of a binary supermassive black hole involves three stages (Begelman et al. 1980), which are summarized by Merritt & Milosavljević (2005) as follows: (1) As the galaxies merge, the supermassive black holes sink toward the center of the new galaxy via dynamical friction forming a binary; (2) the binary continues to decay mainly due to the interaction of stars on orbits intersecting the binary, which are then ejected at velocities comparable to the binary’s orbital velocity, carrying away energy and angular momentum; (3) finally, if the binary’s separation decreases to the point where the emission of gravitational waves becomes efficient at carrying away the last remaining angular momentum, the supermassive black holes coalesce rapidly. There is circumstantial evidence that most binary black holes merge in less than a Hubble time (Komossa 2003a). Therefore, the most massive systems that are able to coalesce in less than a Hubble time will create the loudest gravitational wave events in the universe (Sesana et al. 2004), which might be detectable by a low-frequency gravitational wave experiment such as the Laser Interferometer Space Antenna (LISA).

Our ability to resolve both supermassive black holes in any given binary system depends on the separation between them, and on their distance from Earth. It is believed that the longest timescales in the evolution of a supermassive binary black hole system leading up to coalescence is the stage in which the system is closely bound ($\sim 0.1 - 10$ pc), meaning that in most of these systems the black hole pair can only be resolved by VLBI observations (see review by Komossa 2003a detailing observational evidence for supermassive black holes binaries). Some source properties like X-shaped radio galaxies and double-double radio galaxies, helical radio-jets, double-horned emission line profiles, and semi-periodic variations in lightcurves have been taken as indirect evidence for compact binary black holes though other explanations are possible. The BL Lacertae Object OJ 287 is a candidate for harboring

a supermassive binary black hole, inferred from the characteristics of its optical lightcurve, which shows repeated outbursts at 11.86 y intervals (Sillanpää et al. 1988). Combining optical as well as radio observations, Valtaoja et al. (2000) presented a new interpretation which suggests that at intervals of 11.86 y, the secondary black hole crosses the accretion disk of the primary black hole, causing a thermal flare visible only in the optical. About a year later, the disturbance propagates down the relativistic jet and results in the growth of new synchrotron-emitting shocks visible both in the optical and radio. The observed 11.86 y period corresponds to the orbital period of the compact binary black hole. Some wider systems have, however, been found more directly. The ultra luminous galaxy NGC 6240, discovered by the Chandra X-ray observatory, was found to have a pair of active supermassive black holes at its center (Komossa et al. 2003b), separated by a distance of 1.4 kpc. Another system that has been known for some time is the double AGN (7 kpc separation) constituting the radio source 3C 75, which was discovered by the VLA to have two pairs of radio jets (Owen et al. 1985).

In this paper we present further observations of the radio galaxy 0402+379, which was discovered by Maness et al. (2004) to contain two central, compact, flat spectrum, variable components (designated C1 and C2), a feature which has not been observed in any other compact source. Maness et al. (2004) remarked upon the unusual properties found in this source and proposed several physical explanations. One possible scenario is for one component to be a foreground or background source, instead of being associated with 0402+379. However, because of the small separation between C1 and C2 (7.3 pc), and because of a faint bridge of radio emission found connecting components C1 and C2, this theory was ruled out. A second explanation was that the nucleus was being gravitationally lensed. However, based on the significant difference in the lightcurves of components C1 and C2, and the close proximity of 0402+379 ($z = 0.055$), this theory was also eliminated. Two other scenarios were proposed by Maness et al. (2004), which could not be conclusively ruled out and remained as possible explanations. The first of these suggest that component C2 could be a knot in the southern jet, with C1 classified as the core. To test this hypothesis we performed high frequency, high resolution Very Long Baseline Array (VLBA¹) observations of 0402+379, designed to resolve any jet component and to look for relative motions. The final explanation is that C1 and C2 are two active nuclei of a supermassive binary black hole system.

Throughout this discussion, we assume $H_0 = 75 \text{ km s}^{-1} \text{ Mpc}^{-1}$, $q_0 = 0.5$, and $1 \text{ mas} = 1.06 \text{ pc}$

¹The National Radio Astronomy Observatory is operated by Associated Universities, Inc., under cooperative agreement with the National Science Foundation.

2. Observations

2.1. VLBA Observations from 2005

VLBA observations were made on 2005 January 24 and June 13 at 0.317, 4.976, 8.410, 15.354, 22.222, and 43.206 GHz. Four IFs with a bandwidth of 8 MHz were observed in 32 channels in both R and L circular polarizations. Four-level quantization was employed at all six frequencies. The net integration time on 0402+379 was 115 minutes at 0.3 GHz, 69 minutes at 5 GHz, 69 minutes at 8 GHz, 122 minutes at 15 GHz, 251 minutes at 22 GHz, and 249 minutes at 43 GHz. Standard flagging, amplitude calibration, fringe fitting, bandpass calibration (using 3C 84 for bandpass calibration and 3C 111 for gain calibration), and frequency averaging procedures were followed in the Astronomical Image Processing System (AIPS; van Moorsel et al. 1996). Opacity corrections were performed for the 22 and 43 GHz data. AIPS reduction scripts described in Ulvestad et al. (2001) were used for a large part of the reduction. All manual editing, imaging, deconvolution, and self-calibration were done using Difmap (Shepherd et al. 1995).

2.2. Archival Observations

To further study this source, we obtained fully-calibrated VLBI data taken in 1990 (Xu et al. 1995), in 1996 (VCS; Beasley et al. 2002), in three epochs (1994, 1996, and 1999) of the CJ Proper Motion Survey (Britzen et al. 2003) and in 2003 (Maness et al. 2004). These data were imaged and modeled in Difmap to aid in analysis of motions, variability, and spectra of 0402+379. Further information regarding these observations can be found in Table 1.

2.3. Green Bank Telescope constraints on H₂O Masers

Observations were made with the GBT on 2005 October 14. We used the 18-22 GHz K-band receiver, which uses dual beams separated by 3' in azimuth. The GBT beamwidth is $\sim 36''$ at 22 GHz, and pointing uncertainties were $\sim 5''$. Pointing was corrected hourly using 0402+379 itself, which has sufficient continuum emission. The telescope was nodded between two positions on the sky such that one beam was always centered on the position of 0402+379 during integration. The spectrometer was configured with two bandpasses of 200 MHz each, overlapped by 20 MHz at the redshifted H₂O frequency of 21.075 GHz, so that the total coverage was ± 2700 km s⁻¹ with respect to the systemic velocity of the galaxy.

The spectral resolution was equivalent to 0.33 km s^{-1} . The zenith system temperature was between 40 and 55 K for the duration of the run. Atmospheric opacity at 22 GHz was estimated from system temperature and weather data, and ranged from 0.09 to 0.12 at the zenith. The data were reduced using GBTIDL. We found that the higher frequency IF was subject to a 60 MHz ripple across the baseband, most likely the result of known imperfections and temperature sensitivities of the IF transmission. To reduce the effects of the bandpass ripple we subtracted polynomials of order 4 and 8 from the first and second IFs respectively. We were left with some small residual ripples, but the period of 60 MHz is large enough that any maser emission present would have been apparent nonetheless. We Hanning-smoothed the spectra following calibration. The 1σ rms sensitivity of these observations is $\sim 2 \text{ mJy}$ per km s^{-1} . No maser emission was detected.

2.4. HET Spectroscopy

We obtained a spectrum of the core of 0402+379 on 2004 December 11 with the 9.2m Hobby-Eberly telescope (HET; Ramsey et al 1998) Marcario Low Resolution Spectrograph (LRS; Hill et al. 1998). Two 600s exposures were taken, using the G3 VPH Grism, a Schott OG 515 blocking filter and a $1.5''$ slit placed at the parallactic angle. The resulting spectrum covers $\lambda\lambda = 6300 - 9120 \text{ \AA}$ at 5.6 \AA resolution. We applied standard IRAF calibrations and find that the spectrum is similar to that obtained by Stickel et al. (1993), with a reddened continuum and Seyfert 2 emission lines at a redshift of $z = 0.05523(1)$ ($16,460 \text{ km s}^{-1}$).

In Figure 1 we show the $\text{H}\alpha$ region of the spectrum, where the only strong lines are present. The lines are resolved with Gaussian width $12.5 \pm 1 \text{ \AA}$, after deconvolution of the instrumental resolution. Here the uncertainty is the range in the fitted linewidths for the various species; this substantially exceeds the statistical error. The lines appear asymmetric with a red shoulder suggesting two components with a $\sim 7 \pm 1 \text{ \AA}$ separation, i.e. a component velocity separation of $\sim 300 \text{ km s}^{-1}$. The residual to the line fit in Figure 1 also shows significant excesses in the line wings, suggesting the presence of a broader $\text{H}\alpha$ component.

2.5. The Host Galaxy

Optical imaging is at present quite limited, but in the Palomar Sky survey images 0402+379 appears as a relatively bright $r = 17.2$ elliptical galaxy embedded in a halo of patchy faint emission, extending to an apparent companion $25''$ to the NE. Line emission (OI & NII) is seen from this region in the HET spectra, suggesting the presence of disturbed

photo-ionized gas. An optical image in Stickel et al. (1993) also shows this faint emission. These authors comment that the elliptical core has a “flat brightness distribution”. The 2MASS (Cutri et al. 2003) J–K color of 0402+379 is 1.757, and this is consistent with the value expected for quasars at 0402+379’s redshift (Barkhouse & Hall 2001) The J–K color could indicate star formation activity from a recent merger, or an obscured AGN consistent with the radio galaxy identification for this source. Additional optical imaging would be useful to understand the dynamical state of 0402+379’s core and the origin of the excitation of the surrounding nebulosity.

A source appears near 0402+379 in the ROSAT Bright source catalog (Voges et al. 1999). 1RXSJ040547.3+380308 gives $0.21 \text{ PSPC cnts s}^{-1}$. Using the Galactic absorption in this direction $N_H \approx 3 \times 10^{21} \text{ cm}^{-2}$, and assuming a typical AGN power law index of $\Gamma = 1.7$ this corresponds to an unabsorbed 0.1-2 keV flux of $8.5 \times 10^{-12} \text{ erg cm}^{-2} \text{ s}^{-1}$ or a luminosity $L_{0.1-2} \approx 5 \times 10^{43} \text{ erg s}^{-1}$, i.e. $\sim 2 \times 10^{-26} \text{ erg cm}^{-2} \text{ Hz}^{-1}$. The radio flux density of 0402+379 at 5 GHz is 1.1 Jy (Pauliny-Toth et al. 1978; Becker et al. 1991) which is a radio luminosity of $7 \times 10^{31} \text{ ergs sec}^{-1} \text{ Hz}^{-1}$. This is in agreement with the X-ray to 5 GHz radio luminosity correlation of Brinkmann et al. (2000).

The ROSAT archive also contains two HRI pointings of this source for a combined exposure of 27 ks. These show that the X-ray source is largely resolved, extending over a radius of $\sim 15''$ and appears to follow the faint diffuse emission surrounding the galaxy core. The bulk of the X-ray flux lies between the elliptical and its companion, further supporting the interaction hypothesis. The X-ray luminosity for this diffuse emission is comparable to the AGN estimate above, e.g. $L_{0.1-2} \approx 3 \times 10^{43} \text{ erg s}^{-1}$ for a 1 keV Raymond-Smith plasma, and likely dominates the flux of the ROSAT All-Sky Survey source.

We find that the X-ray emission of 0402+379 is unique; of the 35 known CSO’s (Compact Symmetric Objects) this is the only source detected in the ROSAT All-Sky Survey. Thus, further X-ray observations could abet optical data in probing the nature of this emission and the connection with recent merger and/or nuclear activity.

3. Results

3.1. Radio Continuum

Figure 2 shows naturally weighted 0.3 and 5 GHz images from the 2005 VLBA observations. The structure of the source at 5 GHz reveals the presence of two diametrically opposed jets, as well as two central strong components, one directly between the jets and the other one also between the jets but offset from the center. Following the convention

established by Maness et al. (2004), we designated the aligned central component as C2, and the offset central component as C1. As we can see in Figure 2, the 5 GHz image spans ~ 40 mas (~ 40 pc), corresponding to a small region in the central part of the 0.3 GHz image, which shows structure on scales of ~ 500 mas (~ 500 pc). The orientation of the 0.3 GHz image is consistent with that seen by the VLA at 5 GHz (Maness et al. 2004). The VLA image shows extended emission going northwards, whereas the northern jet seen in our 5 GHz image is pointing in the northeast direction, suggesting that at some point the jet changes direction and starts moving northwards, probably as a consequence of interactions with the surrounding medium. The VLA 1.5 GHz image (Maness et al. 2004) also shows the extended emission going northwards. The southern jet seen in our 5 GHz image is pointing in the southwest direction, which is consistent with both the 1.5 GHz and the 5 GHz VLA images.

Figure 3 shows naturally weighted 8, 15, 22, and 43 GHz images from the 2005 VLBA observations. For both the 8 and 15 GHz images, the overall structure of the source is similar to that at 5 GHz, both jets are present as well as the two central components (C1 and C2).

It is clear that for higher frequencies the two central components are easily distinguished and remain unresolved, while both jets become fainter and are heavily resolved. At 22 GHz these effects are readily apparent, and become more prominent at 43 GHz, where the jets can barely be detected. Before these observations were made, the highest frequency for which data had been taken for this source was 15 GHz.

Elliptical or circular Gaussian components were fitted to the visibility data using Difmap. We obtained an estimate for the sizes of C1 and C2 based on our 15, 22, and 43 GHz model fits. In this case, we fit circular Gaussian components for both C1 and C2, obtaining an average value of 0.173 ± 0.045 mas or 0.183 ± 0.048 pc for C1, and 0.117 ± 0.033 mas or 0.124 ± 0.035 pc for C2.

3.2. Component Motions and Variability

In order to explore questions pertaining to motion and variability in 0402+379, we obtained fully calibrated 5 GHz VLBI data taken in 1990 (Xu et al. 1995), as well as 5 GHz VLBA data taken in three epochs (1994, 1996, and 1999) of the CJ Proper Motion Survey (Britzen et al. 2003) and in 2003 (Maness et al. 2004). Combining these data with our 2005 observations at 5 GHz, we were able to probe motion and variability in this source over a time baseline of 15 y.

Motion and variability studies were performed by fitting eight elliptical Gaussian com-

ponents in Difmap to the 2003 visibility data. Then, we used this model to fit the 5 GHz data corresponding to the 1990, 1994, 1996, 1999, and 2005 epochs. We let only position and flux density vary; all other parameters were held fixed at the 2003 values. Results from our fits are listed in Table 2, and Figure 4 shows the components model, where we have labeled each of them and we also added arrows showing the direction of motion of each component, which will be explained below.

To study component variability in 0402+379, we compared the flux density for components C1 and C2, the mean flux density of the southern components (S1, S2, S3, and S4), and the mean flux density of the northern components (N1 and N2) over each of our 6 epochs at 5 GHz. The above regions were chosen primarily on the basis of their isolation relative to other components in the source. Errors for each region were computed on the basis of the rms noise and our estimated absolute flux calibration errors ($\sim 20\%$ for the 1990 and 1994 Mk II VLBI epochs, and $\sim 5\%$ for the 1996, 1999, 2003, and 2005 VLBA epochs). The resulting fractional variation light curves are shown in Figure 5. These light curves were created by dividing each region’s flux density at each epoch by the mean region flux density found from averaging all epochs. To aid in readability of our graph, the aligned component (C2), the northern lobe, and the southern lobe are displaced on the y -axis by 1, 2, and 3 units, respectively.

From Figure 5 and Table 2 we find that component C1 substantially increases in flux over the 15 y baseline, starting from 18 mJy in 1990 and increasing in brightness to 59 mJy in 2005. We also find that component C2 is variable, ranging from less than 10 mJy in 1990, to 24 mJy in 1996, and 20 mJy in 2005. Because our 1990 epoch was observed with Mk II VLBI, this apparent variability could be in part attributed to poor data quality. However, the measured flux for all other components in 1990 is quite consistent with that in our later epochs, suggesting that the calculated upper limit for component C2’s flux in 1990 is reliable and that the observed variability in this component is significant. For the southern and northern components, we find that there is no substantial variation in the fluxes over the 15 y baseline.

Based on the time variability observed in both C1 and C2 we can estimate the size of these components. However, in this case the variability time scale found for C1 and C2 is quite long (roughly 5 to 10 y), which gives a weak upper limit on the sizes of the components of a few parsecs, consistent with the estimate made in §3.1.

To calculate the relative velocity of the components, we chose component C1 as the reference, based on its strength, compactness, and isolation relative to other components in the source. We compared the relative motion for each epoch by fitting a line to each component’s relative position, split into x and y components, as a function of time. Results

of this fitting process are listed in Table 3, and plotted in Figure 6.

The results of this analysis reveal significant motion for the northern hot spots N1 and N2, yielding a value of 0.054 ± 0.008 mas/y, or $(0.185 \pm 0.008)c$, and 0.033 ± 0.006 mas/y, or $(0.114 \pm 0.019)c$ respectively. These results show that the northern jet is moving away from the two central components to the northeast.

For the southern components S2 and S3, significant motion was also found, yielding 0.0073 ± 0.0025 mas/y, or $(0.0251 \pm 0.0085)c$, and 0.016 ± 0.003 mas/y, or $(0.056 \pm 0.010)c$ respectively. For the other two southern components, S1 and S4, even though the values found for the velocities were larger than those found for S2 and S3, the values obtained in the fitting for χ^2 were large, a fact that can be verified by looking at Figures 6(d) and 6(g). However, for the projected x position of component S4 with time, the χ^2 obtained was nearly unity, which gives us some confidence in the motion of this component, at least in the x direction. We conclude then that, on average, the southern jet is moving away from the two central components to the southwest, though more slowly than the northern jet.

The results obtained for C2 show no significant motion. The value obtained for the limit on the motion of this component is equal to 0.0067 ± 0.0094 mas/y, or less than $0.088c$.

In Figure 4 we draw arrows showing the direction of motion found for each component, as well as their relative magnitude. It is important to note that we placed arrows even for those components for which we do not claim significant motion.

3.3. Radio Continuum Spectra

By appropriately tapering our 22 GHz 2005 data, we obtained an image resolution matched to our 8 GHz continuum image. These two images were then combined to generate an image of the spectral index distribution across the source (Figure 7). In both hotspots of the source, N2 and S2, a steep spectrum was found, whereas in both central components, the spectrum is flat. A plot of flux density as a function of frequency is included in the image of the spectral index distribution for both C1 and C2. The values for the flux densities used in order to make these plots were measured from matching resolution images. Details regarding these results are listed in Table 4.

4. Discussion

Four possible scenarios were proposed by Maness et al. (2004) in order to explain the unusual properties found in 0402+379. Two of them were ruled out, but the possibility that C1 or C2 was an unusual jet component in a dense ISM could not be conclusively eliminated.

Our high resolution observations confirm the compactness of component C2, and measure a size of 0.124 ± 0.035 pc. C2 is found to have no significant motion, whereas significant flux density variability is found. The spectral peak is shown to be at ~ 10 GHz. It is possible that either or both C1 and/or C2 could be a jet component lit up in a collision with a dense interstellar medium. In this scenario the low observed velocity ($< 0.088c$) is due to the impact with the ISM, and the spectrum is modified by local acceleration of particles. Difficulties with the jet component explanation are (1) it requires a dramatic change in the jet axis on timescales of a few 10s of years, while the larger scale emission (see Figure 2) indicates that the jet axis has been fairly stable on time scales up to 10^4 y; (2) a large gradient in density needs to be invoked to decelerate C1 and/or C2 but allow the hotspots to advance (Maness et al. 2004); (3) if C2 is the core responsible for the observed jets and hot spots, and C1 is a jet component, then the counterjet is conspicuous in its absence given the orientation of the source close to the plane of the sky indicated by the source symmetry.

The absence of a jet associated with C1 might at first seem unusual since only 6 of 87 (7%) sources in the First Caltech-Jodrell Bank VLBI survey (CJ1 - the survey in which 0402+379 was imaged by Xu et al. 1995) show naked cores with no sign of a jet at 5 GHz. At lower flux levels, however, which are more appropriate since C1 by itself would not have made it into the CJ1 sample, the fraction of naked cores increases to 6 of 24 sources (25% - Taylor et al. 2005). Thus the absence of a jet from C1 is not by itself evidence against the identification of C1 as an AGN.

The characteristics found in C1 and C2 are typical of AGN; in a complete survey of 32 sources imaged at 43 GHz, (Lister 2001) found no unresolved, isolated jet components. This, together with the morphology of 0402+379, leads us to surmise that neither C1 nor C2 is likely to be a jet component. This leaves the remaining most likely explanation that C1 and C2 are both active black holes in a compact system. For the remainder of the discussion we assume that this is the case and explore what we can learn about such a system from the present observations.

4.1. Constraints on the mass of the black holes

We can use the HET and the VLBA observations to obtain kinematic constraints on the mass of the black hole system. At our observed separation, an orbital velocity of 300 km/s implies a system mass of $1.5 \times 10^8 (v/300 \text{ km s}^{-1})^2 (r/7.3 \text{ pc}) M_\odot$. The suggested line splitting from the optical spectra thus implies a mass of a few times $10^8 M_\odot$. If both radio nuclei are also optically active and show comparable emission line strengths, as expected, then the observed Gaussian line widths put a limit on the line FWHM of $\sim 1300 \text{ km s}^{-1}$, implying a limit on the combined black hole mass of $\sim 3 \times 10^9 M_\odot$. Note that the HI absorption profiles of Maness et al. (2004) also found velocity structure of $\sim 1000 \text{ km s}^{-1}$ extending over a transverse distance of $\sim 20 \text{ pc}$. On this scale the mass contribution from gas and stars is not significant, so the limit obtained reflects the mass of the binary black hole system and indicates a high mass system. The implied mass, $\sim 5 \times 10^9 M_\odot$, could be dominated by the AGN, if the absorption occurs in the nuclear region. Alternatively the two velocity systems might be probing line-of-sight velocities in the products of a recent merger.

An alternative estimate for the central compact object mass can be derived from the blue luminosity of the host bulge (Kormendy & Gebhardt 2001). The observed V magnitude of 0402+379 is ~ 18.5 (Wills et al. 1973), after correcting for the Galactic $A_V \sim 1.6$ and a median B-V color index of ~ 0.9 for 484 ellipticals in the Uppsala General Catalogue (UGC), we obtain a B magnitude of 17.8. This corresponds to a central compact object mass of $\sim 7 \times 10^7 M_\odot$, in reasonable accord with the estimates above, given that this may still be a disturbed system.

4.2. Supermassive Binary Black Hole Orbital Parameters

Using our system mass estimate equal to $1.5 \times 10^8 M_\odot$ and the projected radial separation between them derived from our 2005 maps (7.3 pc), we find from Kepler's Laws that the period of rotation for such a binary supermassive black hole system should be $\sim 1.5 \times 10^5$ y. This period corresponds to a relative projected velocity between components C1 and C2 of $\sim 0.001 c$. The upper limit found for component C1, $< 0.088c$, is consistent with the expected relative velocity between C1 and C2, assuming a stable, Keplerian orbit. To actually constrain the masses of the black holes would require observations over a longer time baseline (~ 100 y).

4.3. Gravitational Wave Signal

What sort of gravitational wave signal might a binary supermassive black hole in 0402+379 generate? Assuming the current separation is 7.3 pc and the total mass is $1.5 \times 10^8 M_{\odot}$ the natural gravitational wave frequency (Hughes 2003) is approximately 2×10^{-13} Hz. This is well below the expected minimum frequency of LISA. Although 0402+379 may be a long way from generating a detectable gravitational wave signal it may represent a source of noise important for future observations of cosmologically produced gravitational radiation. Ultra low frequency gravitational radiation generated during inflation (Hughes 2003) has an upper limit of 10^{-13} Hz. Thus, a population of black hole binaries like 0402+379 may generate substantial noise which could interfere with the detection of the physics of inflation. An estimate of this noise contribution requires a population synthesis model (e.g., Sesana et al. 2005) which is beyond the scope of this work.

The final stage in the evolution of a binary black hole system is the gravitational radiation stage, where the semimajor axis decreases to the point at which gravitational radiation becomes the dominant dissipative force. A binary black hole on a circular orbit will merge within the time (Peters 1964):

$$t_{\text{merge}}(a) = 5.8 \times 10^6 \left(\frac{a}{0.01 \text{ pc}} \right)^4 \left(\frac{10^8 M_{\odot}}{m_1} \right)^3 \frac{m_1^2}{m_2(m_1 + m_2)} \text{ y}, \quad (1)$$

where m_1 and m_2 are the masses of the black holes, and a is the separation between them, once the system is in the final stage. Using the projected radial separation between the black holes we measure for 0402+379 (7.3 pc) and assuming they both have a mass equal to $\sim 10^8 M_{\odot}$, we obtain a merger time equal to $\sim 10^{18}$ y. Some other loss of angular momentum will be necessary if this system is to merge in less than a Hubble time.

It is not clear whether, at present, dynamical friction losses or gas dissipative effects (see Komossa 2003a , Merritt & Milosavljević 2005) are strong enough to bring the binary to the gravitational radiation loss regime within a Hubble time. This relates to the issue of the probability of catching the binary at its present (modest) separation. Are we seeing a recent merger in the act of core coalescence or has the binary stalled and must now await loss-cone replenishment and/or re-supply of nuclear gas? The fact that both nuclei are active (radio bright) suggests on-going accretion and implies dissipation today. Only a larger sample of imaged active nuclei can address the fraction of the population in this state, for example the VLBA Imaging and Polarization Survey (VIPS, Taylor et al. 2005) which will image 1169 sources.

4.4. Jet Components

Assuming that C2 is the origin of the radio emission on parsec scales, we can constrain the orientation of 0402+379. In the simple beaming model for simultaneously ejected jet components moving in opposite directions, both the arm length ratio D and the flux density ratio R depend on the intrinsic speed $\beta = v/c$ and the angle of the twin jets to the line of sight θ (Taylor & Vermeulen 1997). The arm length ratio, D , is given by

$$D = \frac{\mu_N}{\mu_S} = \frac{d_N}{d_S} = \left(\frac{1 + \beta \cos \theta}{1 - \beta \cos \theta} \right), \quad (2)$$

where the apparent projected distances from C2 (assumed to be the origin of radio emission) are d_N for the northern jet (approaching side) and d_S for the southern jet (receding side), and the apparent proper motions are μ_N for the northern jet and μ_S for the southern jet. Similarly, the flux density ratio, R , between the northern and southern jet is

$$R = \frac{S_N}{S_S} = \left(\frac{1 + \beta \cos \theta}{1 - \beta \cos \theta} \right)^{k-\alpha}, \quad (3)$$

where α is the spectral index, $k = 2$ for a continuous jet, and $k = 3$ for discrete jet components (c.f. Lind & Blandford 1985).

In order to determine the arm length ratio we calculated the distances from N2 and S2 to C2 (using the values shown in Table 2), yielding a value of $D = d_N/d_S = 2.42$.

For the proper motion ratio we proceeded as follows. We determined a flux density weighted average velocity, for both the northern and southern components, with respect to C2, using the values shown in Table 3 (calculating the x and y components separately and then calculating the resultant value). Following this procedure we obtained a value of $\mu_N/\mu_S = 6.12$.

The flux density ratio was obtained dividing the sum of the fluxes of the northern components by the sum of the fluxes of the southern components (see Table 2), yielding a value of $S_N/S_S = 0.32$.

If Doppler boosting dominates the appearance of 0402+379 then all the ratios calculated should be in agreement according to Equations 2 and 3. However, using $k = 2$ and estimating a value for the spectral index of both the north and south hotspots of $\alpha = -1$ (see Table 4), we find that $D = 2.42$, $\mu_N/\mu_S = 6.12$, and $R^{\frac{1}{k-\alpha}} = 0.68$, results that are far from agreement, thus ruling out Doppler boosting as the dominant effect. A possible explanation

for this discrepancy could be an enhancement in the density of the interstellar medium to the south of the core, which will reduce the velocity in that direction; slow the expansion over time, thus changing the arm length ratio; and increase the flux density of the southern jet. Additional supporting evidence for this hypothesis comes from the enhancement in HI opacity to the southwest (Maness et al. 2004). Assuming that the density enhancement is a recent phenomenon, we can use the arm length ratio obtained in addition to Equation 2 to get $\beta \cos \theta = 0.4$. This result implies that the intrinsic velocity must be at least $0.4c$ and θ must be less than 66° .

Using the relative velocity between the northern and southern jets (calculated from the values obtained for the flux density weighted averaged velocities of both the southern and northern components) as well as the distance between components S2 and N2, we estimated the age of the current radio emission to be ~ 500 y. If the slower jet velocities for the southern jet are used then the age for the southern lobe is three times as large. Note that these jet ages are much less than the $\sim 10^5$ y binary period in §4.2, so we expect no significant orbital displacement of the jet components.

5. Conclusion

Based on the compactness, motion, variability, and spectra of the two central components in 0402+379 we conclude that they are both active nuclei of a single galaxy. This pair of AGN forms the closest binary black hole system yet discovered with a projected separation of 7.3 pc. The total mass of the system is estimated to be $1.5 \times 10^8 M_\odot$, and the gravitational radiation frequency to be 2×10^{-13} Hz. Energy losses due to gravitational radiation are not yet significant, so that other mechanisms must be invoked if the orbit is to decay. 0402+379 may be the tip of an iceberg for a population of supermassive black hole binaries with parsec scale separations. Such a population may produce significant gravitational wave radiation which may need to be considered for the detection of gravitational radiation in the ultra to very low frequency bands.

Having found one system in the CJF sample (Taylor et al. 1996) of 293 sources, we might expect to find others in a larger survey. The VIPS (Taylor et al. 2005) will image 1169 sources and hopefully find additional compact binary black holes.

Facilities: VLBA, GBT, HET

We thank an anonymous referee for constructive comments. This research has made use of the NASA/IPAC Extragalactic Database (NED) which is operated by the Jet Propulsion

Laboratory, Caltech, under contract with NASA. The National Radio Astronomy Observatory is a facility of the National Science Foundation operated under a cooperative agreement by Associated Universities, Inc.

REFERENCES

Barkhouse, W. A., & Hall, P. B. 2001, AJ, 121, 2843

Beasley, A. J., Gordon, D., Peck, A. B., Petrov, L., MacMillan, D. S., Fomalont, E. B., & Ma, C. 2002, ApJS, 141, 13

Becker, R. H., White, R. L., & Edwards, A. L. 1991, ApJS, 75, 1

Begelman, M. C., Blandford, R. D., & Rees, M. J. 1980, Nature, 287, 307

Brinkmann, W., Laurent-Muehleisen, S. A., Voges, W., Siebert, J., Becker, R. H., Brotherton, M. S., White, R. L., & Gregg, M. D. 2000, A&A, 356, 445

Britzen, S., et al. 2003, Future Directions in High Resolution Astronomy: A Celebration of the 10th Anniversary of the VLBA, edited by J. D. Romney and M. J. Reid. Socorro, N.M. : National Radio Astronomy Observatory, 2003., p.85, 85

Cutri, R. et al. 2003, 2MASS Extended Source Catalog, NASA/IPAC Extragalactic Database

Filippenko, A. V., & Ho, L. C. 2003, ApJ, 588, L13

Gebhardt, K., Rich, R. M., & Ho, L. C. 2005, ApJ, 634, 1093

Hill, G. J., Nicklas, H. E., MacQueen, P. J., Tejada, C., Cobos Duenas, F. J., & Mitsch, W. 1998, Proc. SPIE, 3355, 375

Hughes, S. A. 2003, Annals of Physics, 303, 142

Komossa, S. 2003, AIP Conf. Proc. 686: The Astrophysics of Gravitational Wave Sources, 686, 161

Komossa, S., Burwitz, V., Hasinger, G., Predehl, P., Kaastra, J. S., & Ikebe, Y. 2003, ApJ, 582, L15

Kormendy, J., & Gebhardt, K. 2001, AIP Conf. Proc. 586: 20th Texas Symposium on relativistic astrophysics, 586, 363

Lister, M. L. 2001, ApJ, 562, 208

Lind, K. R., & Blandford, R. D. 1985, *ApJ*, 295, 358

Maness, H. L., Taylor, G. B., Zavala, R. T., Peck, A. B., & Pollack, L. K. 2004, *ApJ*, 602, 123

Merritt, D., & Milosavljević, M. 2005, *Living Reviews in Relativity*, 8, 8

Owen, F. N., Odea, C. P., Inoue, M., & Eilek, J. A. 1985, *ApJ*, 294, L85

Pauliny-Toth, I. I. K., Witzel, A., Preuss, E., Kühr, H., Fomalont, E. B., Davis, M. M., & Kellermann, K. I. 1978, *AJ*, 83, 451

Peters, P. C. 1964, *Phys. Rev. B*, 136, 1224

Ramsey, L. W., et al. 1998, *Proc. SPIE*, 3352, 34

Richstone, D., et al. 1998, *Nature*, 395, A14

Sesana, A., Haardt, F., Madau, P., & Volonteri, M. 2004, *ApJ*, 611, 623

Sesana, A., Haardt, F., Madau, P., & Volonteri, M. 2005, *ApJ*, 623, 23

Shepherd, M. C., Pearson, T.J., & Taylor, G.B. 1995, *BASS*, 27, 903

Sillanpää, A., Haarala, S., Valtonen, M. J., Sundelius, B., & Byrd, G. G. 1988, *ApJ*, 325, 628

Stickel, M., Kuehr, H., & Fried, J. W. 1993, *A&AS*, 97, 483

Taylor, G. B., Readhead, A. C. S., & Pearson, T. J. 1996, *ApJ*, 463, 95

Taylor, G. B., & Vermeulen, R. C. 1997, *ApJ*, 485, L9

Taylor, G. B., et al. 2005, *ApJS*, 159, 27

Ulvestad, J., Greisen, E. W. & Mioduszewski, A. 2001, AIPS Memo 105:AIPS Procedures for initial VLBA Data Reduction, NRAO

Valtaoja, E., Teräsranta, H., Tornikoski, M., Sillanpää, A., Aller, M. F., Aller, H. D., & Hughes, P. A. 2000, *ApJ*, 531, 744

van Moorsel, G., Kemball, A., & Greisen, E. 1996, ASP Conf. Ser. 101: Astronomical Data Analysis Software and Systems V, 5, 37

Voges, W., et al. 1999, *A&A*, 349, 389

Wills, B. J., Wills, D., & Douglas, J. N. 1973, AJ, 78, 521

Xu, W., Readhead, A. C. S., Pearson, T. J., Polatidis, A. G., & Wilkinson, P. N. 1995,
ApJS, 99, 297

Table 1. Observations

Frequency (GHz)	Instrument	Date	Time (min)	BW (MHz)	Pol.	IFs	Peak (Jy/beam)	rms (mJy)	Reference
0.32	VLBA	2005 Jun 13	115	8	2	4	0.32	0.59	This paper
4.99	VLBI Mk 2	1990 Mar 10	80	2	1	1	0.17	0.94	Xu et al. 1995
4.99	VLBI Mk 2	1994 Sep 17	57	2	1	1	0.17	1.6	Britzen et al. 2003
4.99	VLBI	1996 Aug 19	41	8	1	1	0.16	0.63	Britzen et al. 2003
4.99	VLBA	1999 Nov 26	35	8	2	2	0.18	0.42	Britzen et al. 2003
5.00	VLBA	2003 Mar 02	478	16	2	1	0.16	0.21	Maness et al. 2003
4.98	VLBA	2005 Jan 24	69	8	2	4	0.13	0.12	This paper
8.41	VLBA	2005 Jun 13	69	8	2	4	0.06	0.06	This paper
15.35	VLBA	2005 Jan 24	122	8	2	4	0.05	0.17	This paper
22.22	VLBA	2005 Jun 13	251	8	2	4	0.03	0.22	This paper
43.21	VLBA	2005 Jan 24	249	8	2	4	0.02	0.25	This paper

Table 2. Gaussian Model Components* .

Component	Epoch	S (Jy)	r (mas)	θ ($^{\circ}$)	a (mas)	b/a	Φ ($^{\circ}$)	χ^2
C1...	1990.185	0.018 ± 0.004	0.0	0.0	0.525	1.00	172.4	1.13
	1994.708	0.040 ± 0.009	0.0	0.0	0.525	1.00	172.4	0.90
	1996.630	0.040 ± 0.003	0.0	0.0	0.525	1.00	172.4	1.31
	1999.899	0.050 ± 0.004	0.0	0.0	0.525	1.00	172.4	1.28
	2003.162	0.060 ± 0.004	0.0	0.0	0.525	1.00	172.4	2.07
	2005.062	0.059 ± 0.003	0.0	0.0	0.525	1.00	172.4	1.67
C2...	1990.185	<0.010						
	1994.708	0.025 ± 0.006	7.323	286.21	1.61	1.00	207.9	0.90
	1996.630	0.024 ± 0.002	6.932	284.58	1.61	1.00	207.9	1.31
	1999.899	0.018 ± 0.001	6.803	282.00	1.61	1.00	207.9	1.28
	2003.162	0.021 ± 0.001	6.809	282.72	1.61	1.00	207.9	2.07
	2005.062	0.020 ± 0.001	6.876	283.40	1.61	1.00	207.9	1.67
S1...	1990.185	0.078 ± 0.017	11.063	254.74	3.29	1.00	308.3	1.13
	1994.708	0.090 ± 0.020	12.154	251.22	3.29	1.00	308.3	0.90
	1996.630	0.087 ± 0.006	11.978	251.46	3.29	1.00	308.3	1.31
	1999.899	0.090 ± 0.006	11.600	251.83	3.29	1.00	308.3	1.28
	2003.162	0.119 ± 0.007	11.846	251.19	3.29	1.00	308.3	2.07
	2005.062	0.103 ± 0.005	11.876	252.10	3.29	1.00	308.3	1.67
S2...	1990.185	0.291 ± 0.064	14.119	248.45	1.51	1.00	302.3	1.13
	1994.708	0.228 ± 0.050	14.364	248.46	1.51	1.00	302.3	0.90
	1996.630	0.211 ± 0.015	14.234	248.71	1.51	1.00	302.3	1.31
	1999.899	0.198 ± 0.014	14.120	248.66	1.51	1.00	302.3	1.28
	2003.162	0.208 ± 0.012	14.165	248.88	1.51	1.00	302.3	2.07
	2005.062	0.159 ± 0.008	14.192	248.84	1.51	1.00	302.3	1.67
S3...	1990.185	0.187 ± 0.041	16.029	253.40	3.40	0.37	32.0	1.13
	1994.708	0.168 ± 0.037	16.144	252.75	3.40	0.37	32.0	0.90
	1996.630	0.158 ± 0.011	16.149	252.48	3.40	0.37	32.0	1.31
	1999.899	0.152 ± 0.011	16.084	252.39	3.40	0.37	32.0	1.28
	2003.162	0.186 ± 0.011	16.015	252.48	3.40	0.37	32.0	2.07
	2005.062	0.153 ± 0.008	15.980	252.48	3.40	0.37	32.0	1.67
S4...	1990.185	0.006 ± 0.001	17.454	251.27	2.72	0.10	333.8	1.13
	1994.708	0.028 ± 0.006	17.399	252.60	2.72	0.10	333.8	0.90
	1996.630	0.019 ± 0.001	17.731	250.16	2.72	0.10	333.8	1.31
	1999.899	0.019 ± 0.001	17.641	248.96	2.72	0.10	333.8	1.28
	2003.162	0.029 ± 0.002	17.763	249.71	2.72	0.10	333.8	2.07
	2005.062	0.027 ± 0.001	17.861	249.79	2.72	0.10	333.8	1.67
N1...	1990.185	0.107 ± 0.024	17.033	5.15	13.58	0.27	20.3	1.13
	1994.708	0.093 ± 0.020	18.678	4.72	13.58	0.27	20.3	0.90
	1996.630	0.086 ± 0.006	19.143	5.95	13.58	0.27	20.3	1.31
	1999.899	0.085 ± 0.006	18.874	5.45	13.58	0.27	20.3	1.28
	2003.162	0.105 ± 0.006	19.271	6.13	13.58	0.27	20.3	2.07
	2005.062	0.091 ± 0.005	19.353	6.15	13.58	0.27	20.3	1.67
N2...	1990.185	0.044 ± 0.010	21.103	12.86	2.38	1.00	254.2	1.13
	1994.708	0.057 ± 0.013	21.414	11.47	2.38	1.00	254.2	0.90
	1996.630	0.049 ± 0.003	21.416	13.17	2.38	1.00	254.2	1.31

Table 2—Continued

Component	Epoch	<i>S</i> (Jy)	<i>r</i> (mas)	θ ($^{\circ}$)	<i>a</i> (mas)	<i>b/a</i>	Φ ($^{\circ}$)	χ^2
	1999.899	0.056 \pm 0.004	21.487	13.15	2.38	1.00	254.2	1.28
	2003.162	0.068 \pm 0.004	21.613	13.42	2.38	1.00	254.2	2.07
	2005.062	0.051 \pm 0.003	21.585	13.39	2.38	1.00	254.2	1.67

*NOTE - Parameters of each Gaussian component of the model brightness distribution are as follows: Component, Gaussian component; Epoch, year of observation (see Table 1 and §1); *S*, flux density; *r*, θ , polar coordinates of the center of the component relative to the center of component C1 (Beasley et al. (2002) calculated the position of the source to be \sim RA 04h05m49.2623s Dec $+38^{\circ}03'32''$.235. We are assuming component C1 to be approximately at this location); *a*, semimajor axis; *b/a*, axial ratio; Φ , component orientation; χ^2 , goodness-of-fit for eight component model in each epoch. All angles are measured from north through east. Errors in flux are based on our absolute amplitude calibration as well as the rms noise. Note that due to the complicated morphology of the source, variability studies were performed using components C1, C2, the sum of the southern components (S1, S2, S3, and S4), and the sum of the northern components (N1 and N2).

Table 3. Component Motion Fitting Results.

Component	Velocity in <i>y</i> (mas/y)	χ^2	Velocity in <i>x</i> (mas/y)	χ^2	Velocity (mas/y)	Velocity (c)	Angle of Motion * ($^{\circ}$)
C1	Reference Component
C2	-0.006 ± 0.007	2.02	0.003 ± 0.007	0.60	0.007 ± 0.009	0.023 ± 0.032	153.4
S1	-0.027 ± 0.003	9.66	-0.024 ± 0.003	6.90	0.036 ± 0.004	0.124 ± 0.015	221.6
S2	0.007 ± 0.002	0.35	-0.002 ± 0.002	1.34	0.007 ± 0.002	0.025 ± 0.009	344.5
S3	-0.013 ± 0.002	1.30	0.010 ± 0.002	0.34	0.016 ± 0.003	0.056 ± 0.010	142.4
S4	-0.016 ± 0.006	5.85	-0.026 ± 0.006	1.04	0.031 ± 0.008	0.105 ± 0.028	238.4
N1	0.046 ± 0.006	1.90	0.028 ± 0.006	1.30	0.054 ± 0.008	0.185 ± 0.028	31.3
N2	0.023 ± 0.004	0.68	0.024 ± 0.004	2.59	0.033 ± 0.006	0.114 ± 0.019	46.2

*Angles measured from north through east.

Table 4. Continuum Spectrum Results* .

Component	Frequency (GHz)	Flux (mJ)	α_{5-8}	α_{8-15}	α_{8-22}	α_{15-22}	α_{22-43}
C1...	4.987	53.2 ± 2.6	0.25 ± 0.19	-0.24 ± 0.25	-0.55 ± 0.15	-1.07 ± 0.54	-0.62 ± 0.30
	8.421	60.5 ± 3.0					
	15.365	52.4 ± 5.2					
	22.233	35.3 ± 3.5					
	43.217	23.4 ± 2.3					
C2...	4.987	10.7 ± 0.5	0.68 ± 0.19	-0.06 ± 0.26	-0.37 ± 0.16	-0.88 ± 0.55	-0.44 ± 0.31
	8.421	15.3 ± 0.8					
	15.365	14.8 ± 1.5					
	22.233	10.7 ± 1.1					
	43.217	8.0 ± 0.8					
S2...	4.987	72.2 ± 3.5	-0.42 ± 0.19	-0.73 ± 0.25	-1.11 ± 0.16	-1.73 ± 0.55	-1.24 ± 0.31
	8.421	57.8 ± 3.0					
	15.365	37.2 ± 3.7					
	22.233	19.6 ± 2.0					
	43.217	8.6 ± 0.9					
N2...	4.987	11.2 ± 0.5	-0.18 ± 0.18	-0.56 ± 0.24	-0.89 ± 0.15	-1.43 ± 0.51	...
	8.421	10.2 ± 0.5					
	15.365	7.3 ± 0.7					
	22.233	4.3 ± 0.4					
	43.217	undetected					

*Results obtained from the 2005 VLBA observations. The fluxes were measured from matching resolution images. See §3.3 for more details.

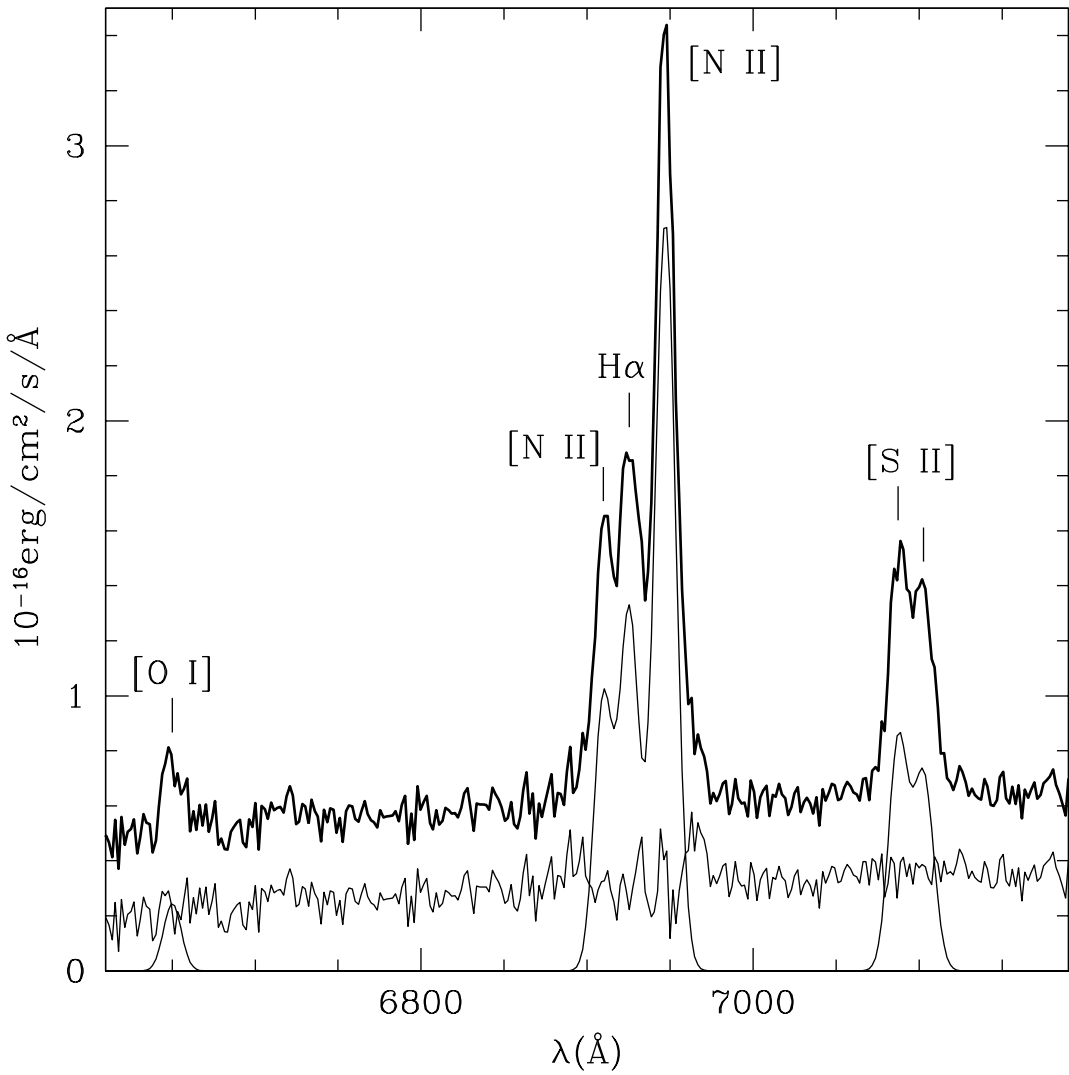


Fig. 1.— The optical spectrum at 5.6 \AA spectral resolution taken by the Hobby-Eberly Telescope. The thick line is the spectrum, the thin line shows the single component model and the residual spectrum.

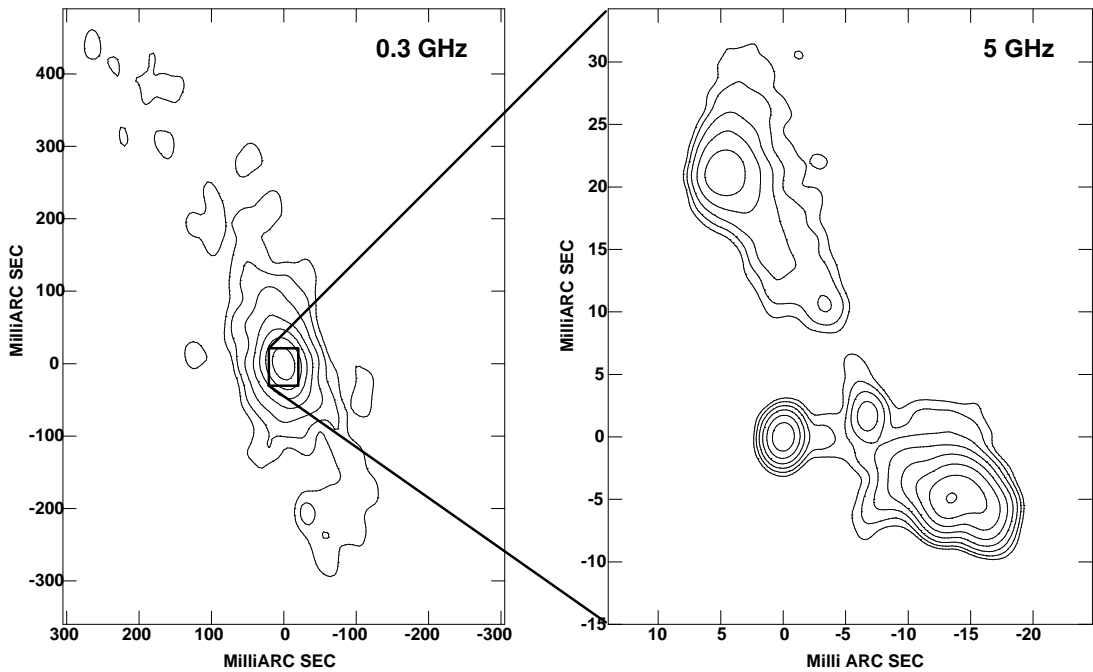


Fig. 2.— Naturally weighted 2005 VLBA images of 0402+379 at 0.3 and 5 GHz. Contours are drawn beginning at 3σ and increase by factors of 2 thereafter. The peak flux density and rms noise for each frequency are given in Table 1. Right ascension and declination are relative to C1, as shown in Figure 3, assumed to be at \sim RA 04h05m49.2623s Dec $+38^{\circ}03'32''.235$ (Beasley et al. 2002).

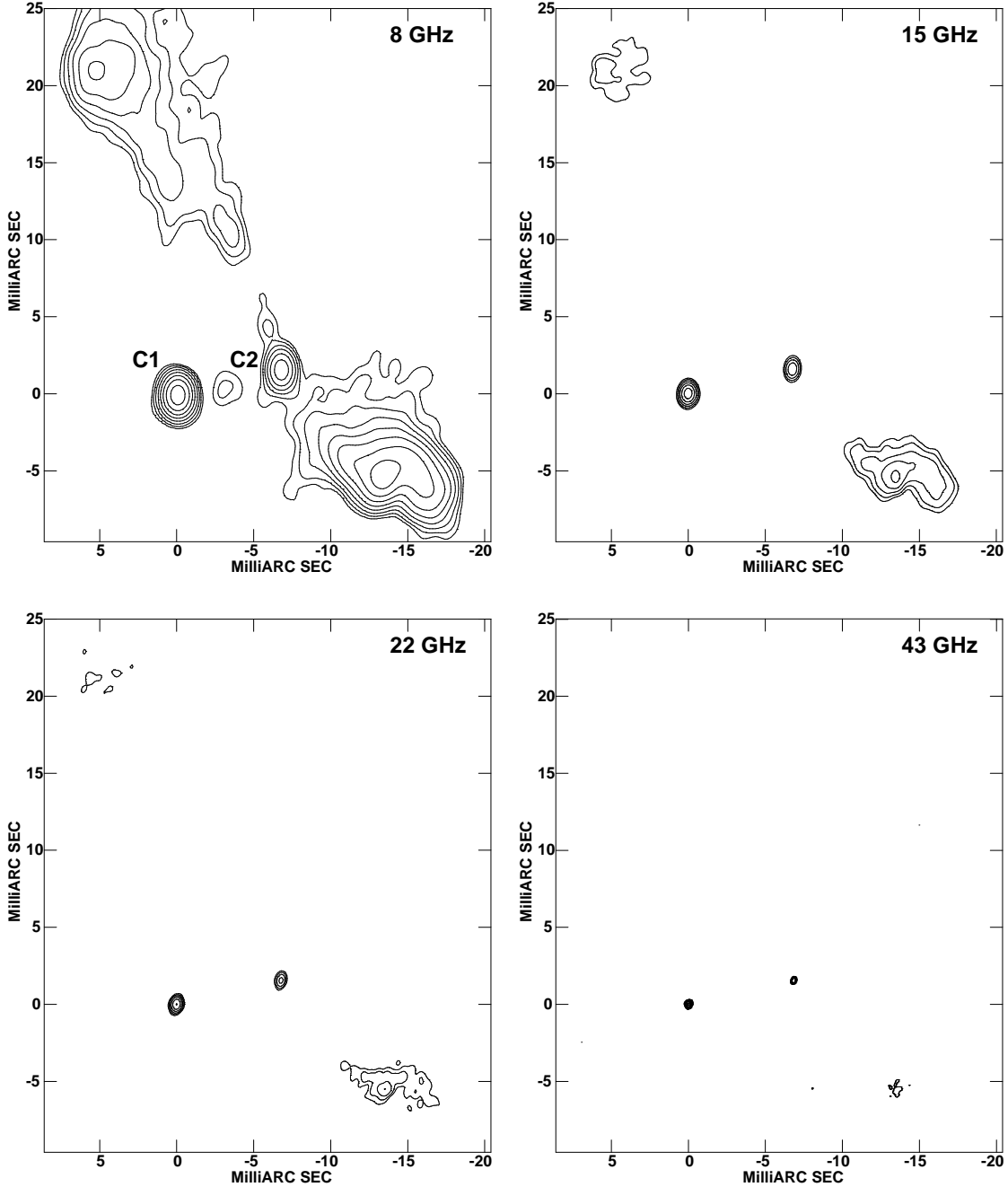


Fig. 3.— Naturally weighted 2005 VLBA images of 0402+379 at 8, 15, 22 and 43 GHz. Contours are drawn beginning at 3σ and increase by factors of 2 thereafter. The peak flux density and rms noise for each frequency are given in Table 1. The labels shown in the 5 GHz map indicate the positions of the two strong, compact, central components derived from model-fitting.

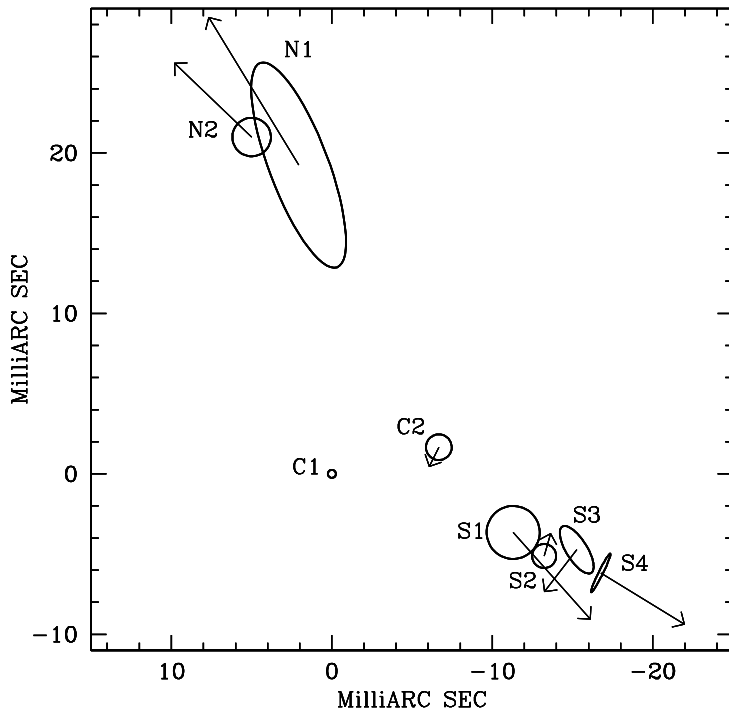


Fig. 4.— Components model for the VLBA observations of 0402+379 at frequencies of 5 GHz and above. The arrows shown represent the direction of motion found for each component, relative to the position of C1, obtained from a time baseline of 15 y. Arrow lengths have been multiplied by a factor of 200. See §3.2 for more details. Note that we placed arrows even for those components for which we are not claiming motion. The specific model shown corresponds to a frequency of 5 GHz.

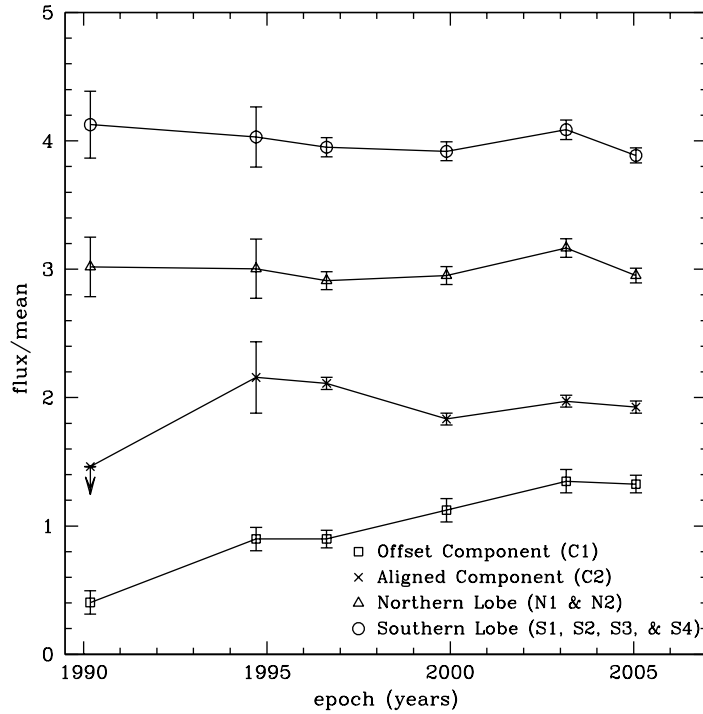


Fig. 5.— Light curves of the different components of 0402+379 at 5 GHz. The flux densities that produced this graph were taken from Table 2 and are discussed in §3.2. The displayed light curves were created by dividing each region’s flux at each epoch by the mean region flux found from averaging all observed epochs. The aligned core candidate, the northern lobe, and the southern lobe are displayed on the y -axis by 1, 2, and 3 units, respectively. Errors are estimated from the rms noise and the absolute flux calibration errors for each epoch.

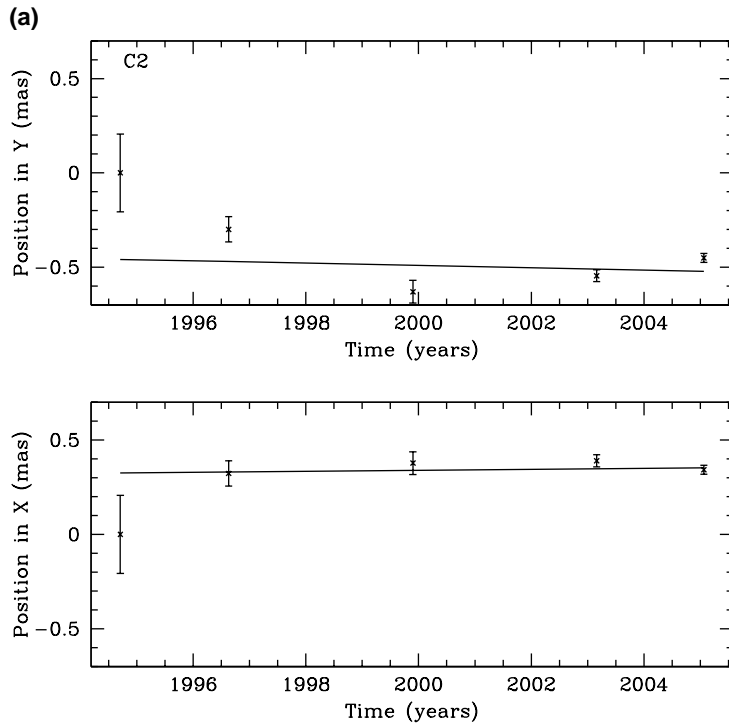


Fig. 6.— (a) Projected x and y positions of component C2 with time. The x and y components of velocity are shown as a solid line. (b) Same for component N1. (c) Same for component N2. (d) Same for component S1. (e) Same plot component S2. (f) Same component S3. (g) Same for component S4. See Table 3 for more details.

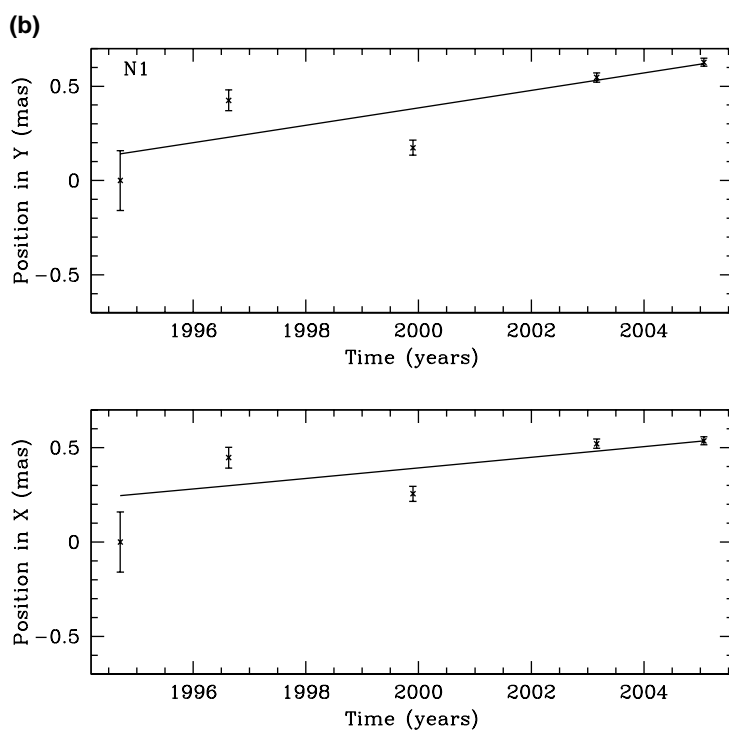


Fig. 6.— Figure 6 continued

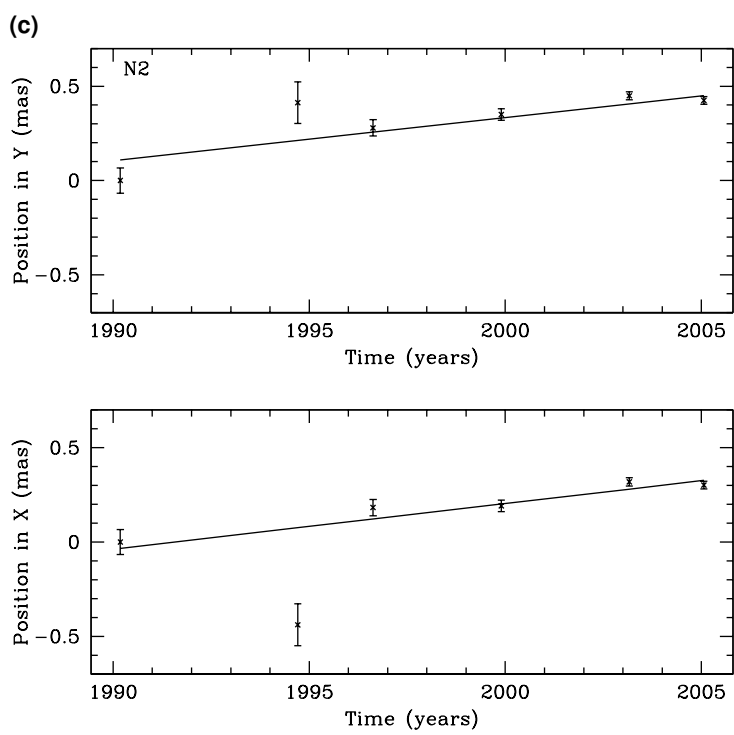


Fig. 6.— Figure 6 continued

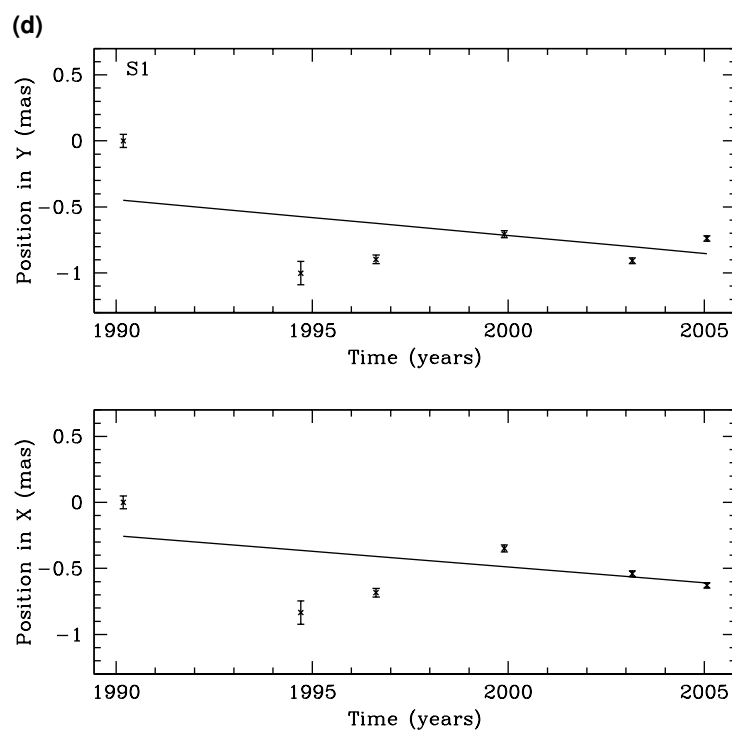


Fig. 6.— Figure 6 continued

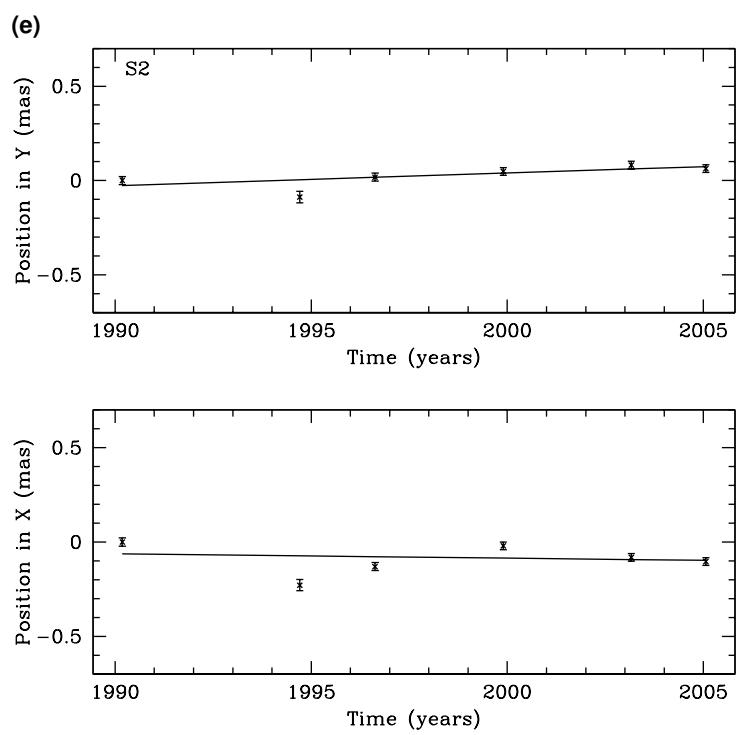


Fig. 6.— Figure 6 continued

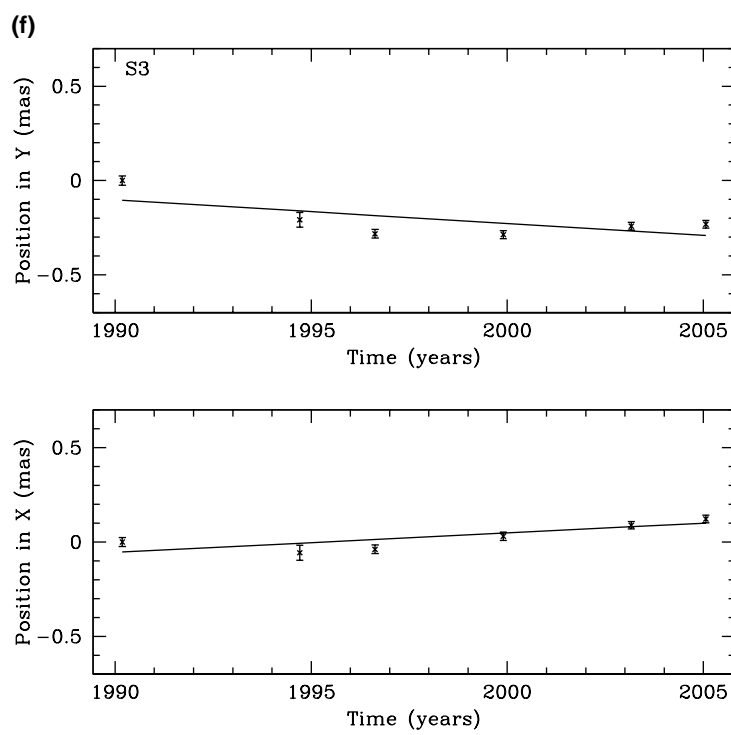


Fig. 6.— Figure 6 continued

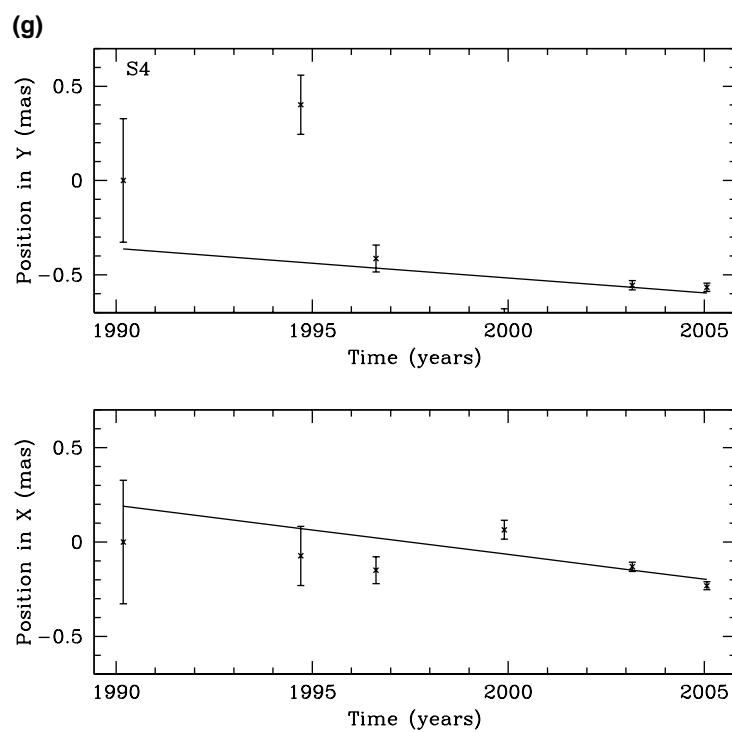


Fig. 6.— Figure 6 continued

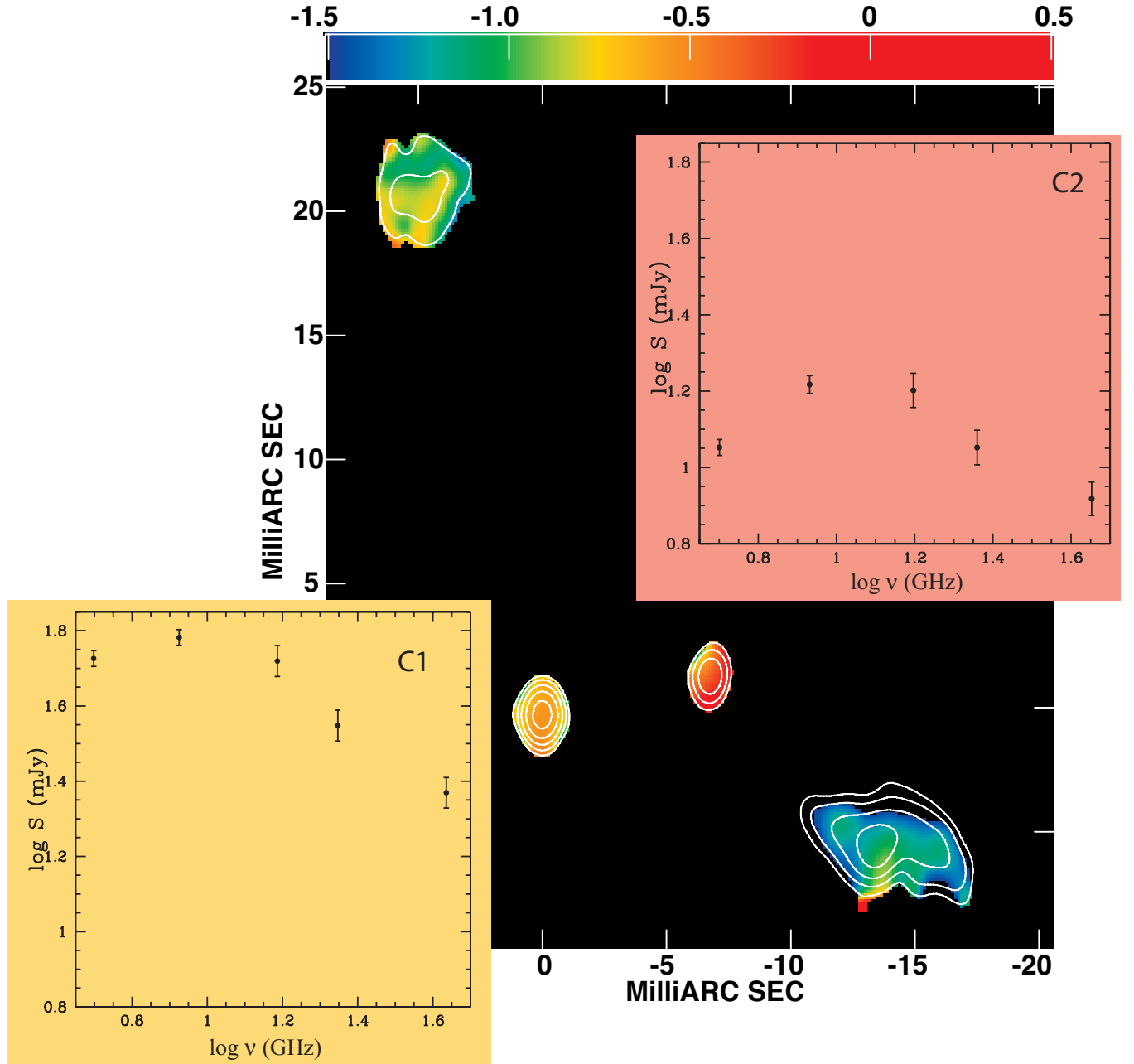


Fig. 7.— Spectral index distribution between 8 and 22 GHz from the 2005 VLBA observations. The contours are taken from the 22 GHz observations and are set at 7σ , increasing by a factor of 2 thereafter.